Science Advances
AAAS

advances.sciencemag.org/cgi/content/full/7/2/eabe3097/DC1

Supplementary Materials for

A thin, deformable, high-performance supercapacitor implant that can be biodegraded and bioabsorbed within an animal body

Hongwei Sheng, Jingjing Zhou, Bo Li, Yuhang He, Xuetao Zhang, Jie Liang, Jinyuan Zhou, Qing Su, Erqing Xie, Wei Lan*, Kairong Wang*, Cunjiang Yu*

*Corresponding author. Email: lanw@lzu.edu.cn (W.L.); wangkr@lzu.edu.cn (K.W.); cyu15@uh.edu (C.Y.)

Published 8 January 2021, *Sci. Adv.* **7**, eabe3097 (2021)
DOI: 10.1126/sciadv.abe3097

This PDF file includes:

Calculations

The areal capacitance for the MoO_x electrodes and the as-fabricated supercapacitor implants was calculated from cyclic voltammetry (CV) and galvanostatic charge-discharge (GCD) profiles based on the following equations, respectively:

$$C_{area} = \frac{1}{2\nu A \Delta V} \oint I(V)\mathrm{d}V \quad (1)$$

$$C_{area} = \frac{\int_{t_0}^{t} i dt}{\Delta V A} \quad (2)$$

where C_{area} is the areal capacitance in F cm^{-2}, ν is the scan rate in V s^{-1}; ΔV is a potential range in V, I(V) is the instantaneous current in CV curves and V is applied voltage in V. i refers to the discharge current; t_o and t are the starting time and end time for discharge process, respectively. And A corresponds to the effective area of the active material layer (MoO_x flakes).

The energy density and power density of the supercapacitor implants were calculated using the following equations:

$$E = \frac{1}{2} \times C_{area} \times \frac{(\Delta V)^2}{3600} \quad (3)$$

$$P = \frac{E}{\Delta t} \times 3600 \quad (4)$$

Where E and P correspond to the areal energy density and power density, respectively. Δt is discharge time.

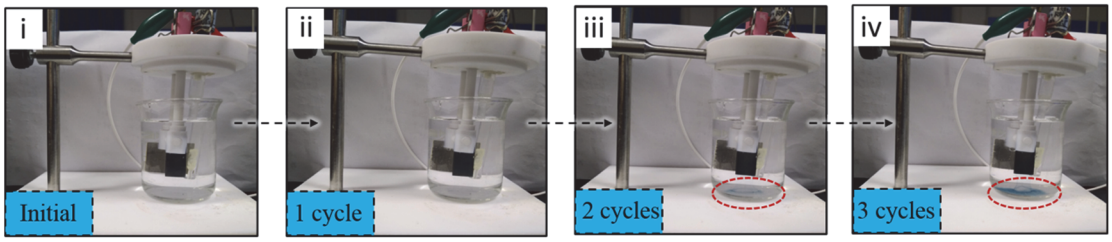

Fig. S1. Optical images of the Mo foil at initial oxidation stage. This process (i-iv) is followed by the continuous corrosion and electro-polishing of Mo foil. Photo credit: Hongwei Sheng, Lanzhou University.

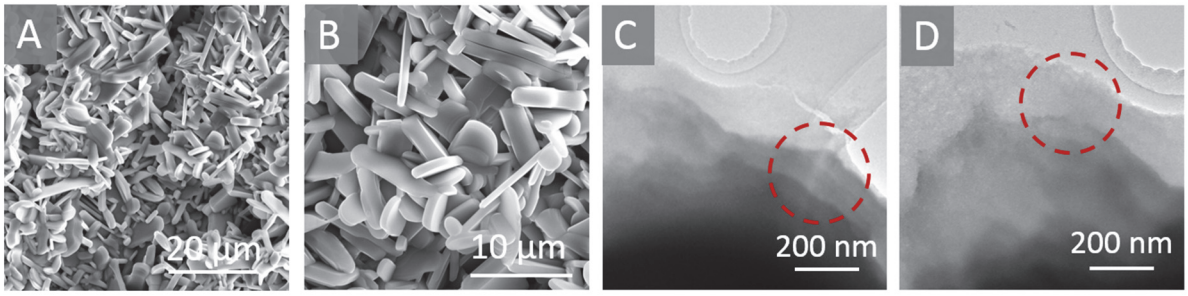

Fig. S2. Morphology of MoO_x electrode and the delaminated MoO_x flakes. (A-B) SEM images of MoO_x electrode at different magnifications. **(C-D)** TEM images of the delaminated MoO_x flakes, indicating an apparent layered structure.

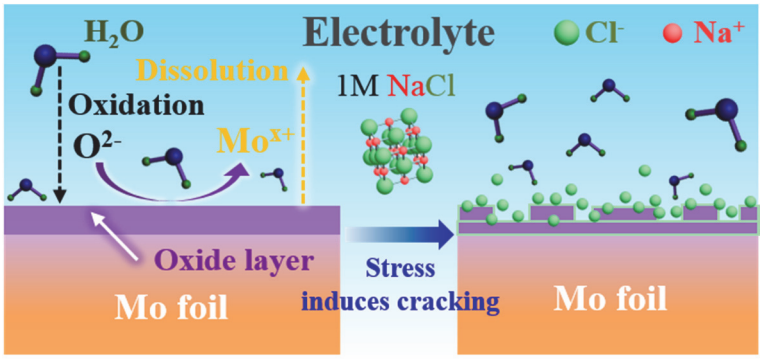

Fig. S3. Schematic illustrating the mechanism of MoO_x micro-blocks formed on Mo foil surface.

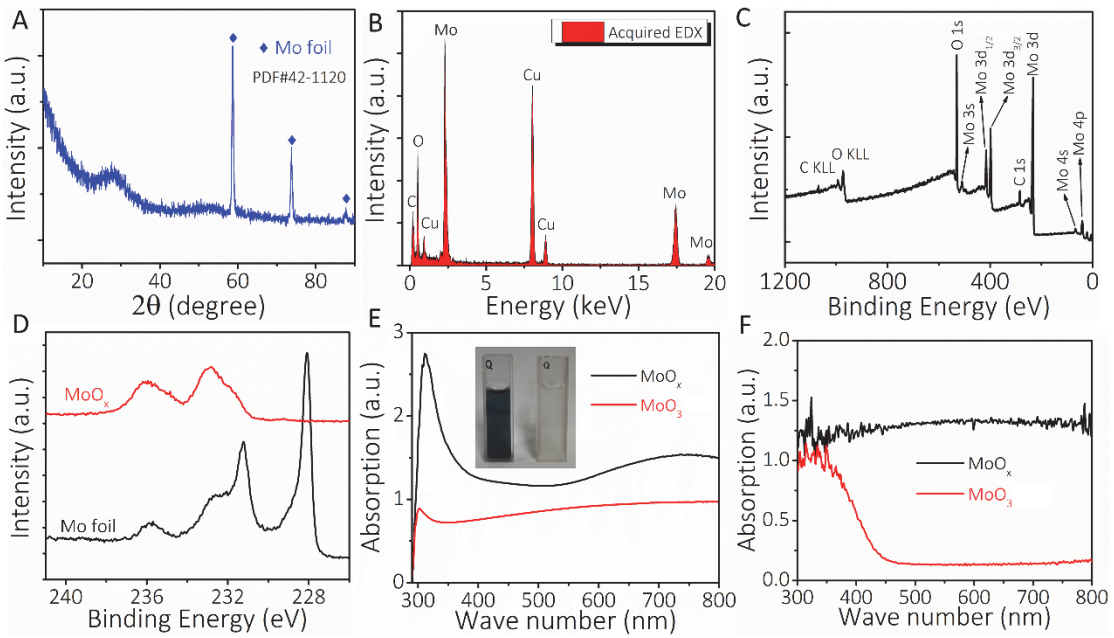

Fig. S4. Spectrum analysis of MoO_x electrode and MoO_x flakes. (A) XRD pattern of the as-synthesized MoO_x electrode. Three intense peaks centered at 40.5, 58.6, and 73.7 ° can be indexed to the (110), (200), and (211) crystal planes of metallic Mo (PDF#42-1120), respectively. **(B)** The acquired EDX spectrum of the delaminated MoO_x flakes. **(C)** XPS survey spectrum of MoO_x electrode. **(D)** Comparison of Mo 3d XPS spectra with MoO_x electrode and pure Mo foil. The corresponding ultraviolet-visible (UV-Vis) absorption spectra of the MoO_x flakes and MoO_3 at **(E)** aqueous solutions and **(F)** powers states. Inset: a digital photograph of MoO_x (left) and MoO_3 (right) aqueous solutions. Photo credit: Hongwei Sheng, Lanzhou University.

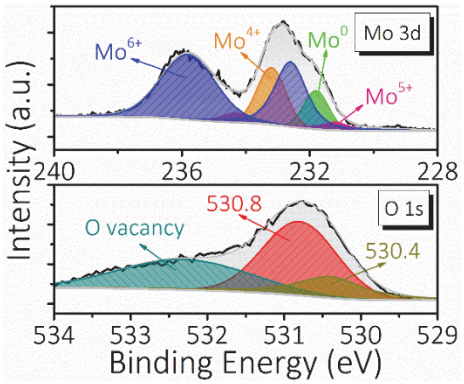

Fig. S5. The core-level XPS spectra of Mo 3d and O 1s of MoO_x flakes.

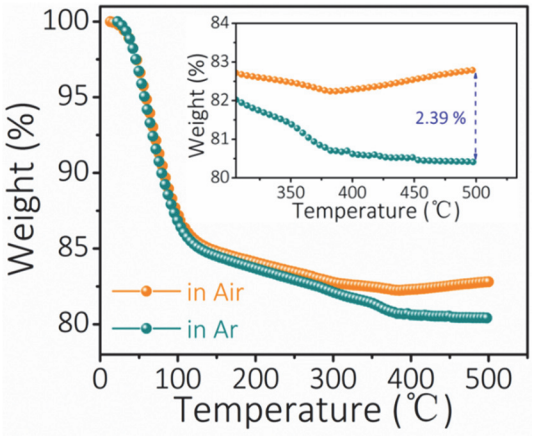

Fig. S6. Thermal gravimetric analysis (TGA) curves for MoO_x (in Air, and Ar). The concentration of oxygen vacancies was calculated from the difference in weight decrease between the two TGA traces.

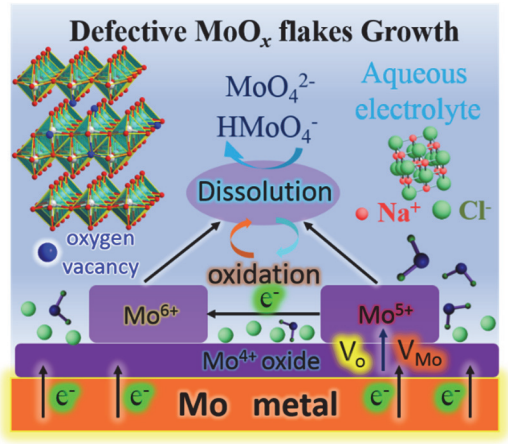

Fig. S7. Schematic of a proposed model for the Mo/oxide film interface during the anodization.

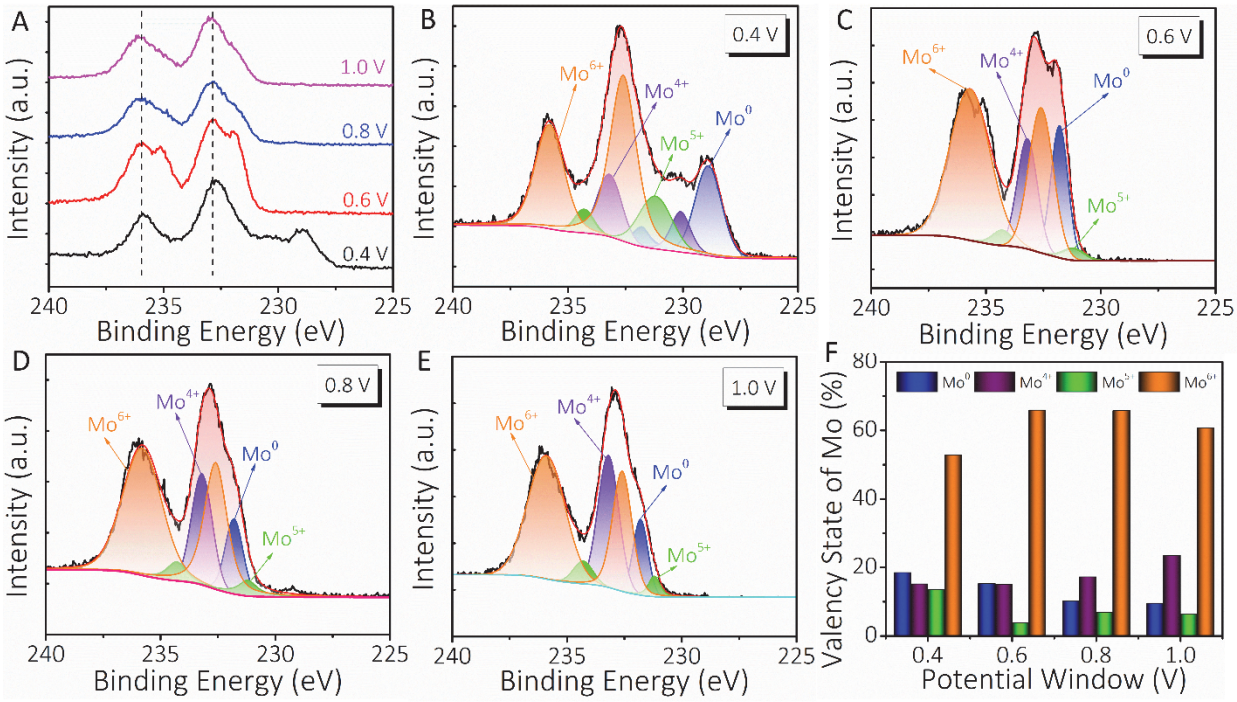

Fig. S8. XPS spectra of Mo 3d for MoO_x flakes anodized at different potential windows. (A) The integrated and **(B-E)** the individual core-level XPS spectra of Mo 3d, and **(F)** the distribution percent of Mo valence states.

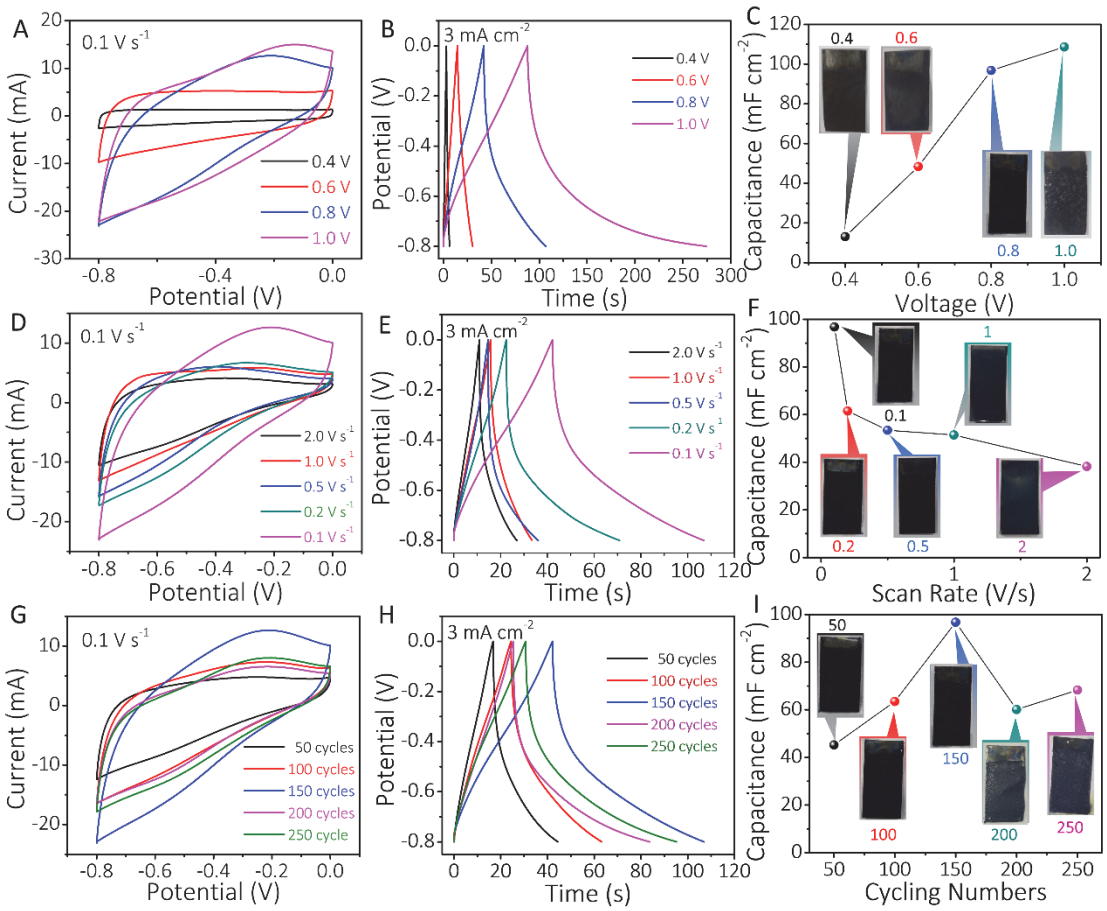

Fig. S9. Electrochemical characterizations of MoO_x electrodes under different oxidation conditions. CV curves (at 0.1 V s^{-1}), GCD curves, and the calculated areal capacitance of MoO_x electrode at **(A-C)** different potential windows, **(D-F)** different scan rates, and **(G-I)** different cycling numbers. The overvoltage anodization made contact between MoO_x flakes and Mo foil weak, resulting in reduced utilization of active materials. Photo credit: Hongwei Sheng, Lanzhou University.

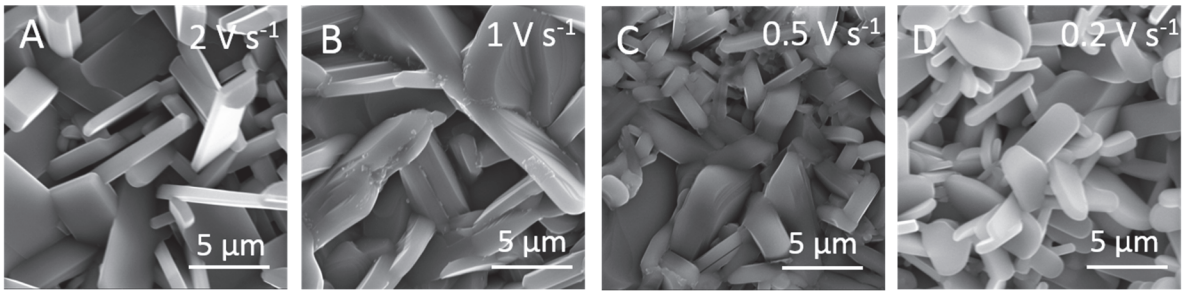

Fig. S10. SEM images of MoO_x electrode (at 0.8 V, 150 cycles) anodized at different scan rates. (A-D) 2, 1, 0.5 and 0.2 V s^{-1}, respectively.

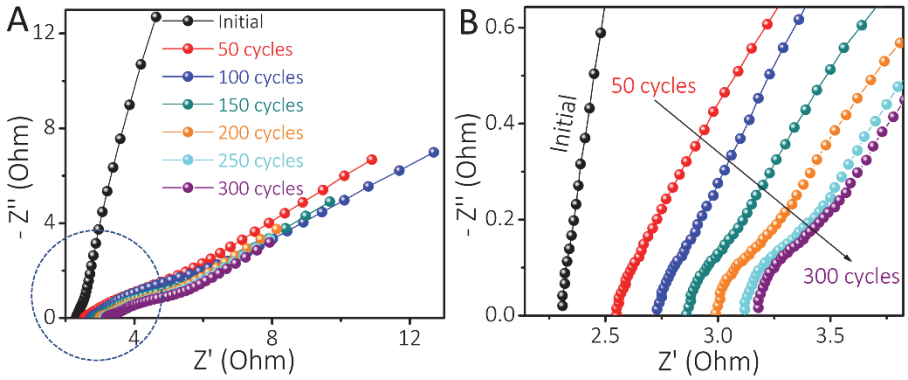

Fig. S11. EIS curves and partial enlargement of MoO_x electrodes (anodized at 0.8 V, 0.1 Vs^{-1}) after different cycling numbers. (A-B) With increasing cycle numbers, the stress induces the partial oxide to fall off from the surface, and the equivalent series resistance (R_s) of MoO_x electrodes also increases.

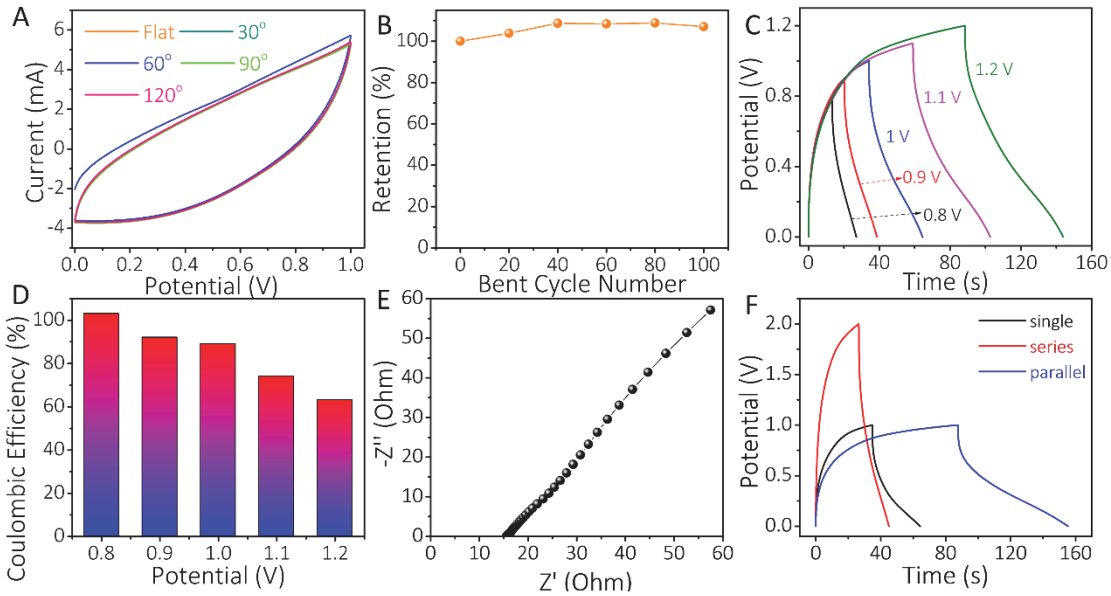

Fig. S12. Electrochemical performances of the supercapacitor impalnt. (A) CV curves (at 0.1 V s^{-1})of MoO_x-based supercapacitors under various bending angles. **(B)** Capacitance retention after bending 100 times. **(C)** GCD curves at 2 mA cm^{-2}, and **(D)** Coulombic efficiency of MoO_x-based supercapacitors under different voltage windows. **(E)** Nyquist plot of MoO_x-based supercapacitor. **(F)** GCD curves (at 2 mA cm^{-2}) of two supercapacitor devices connected in series or parallel.

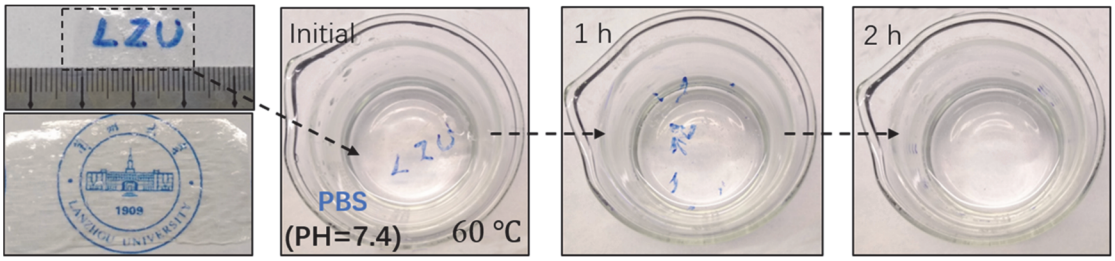

Fig. S13. Time sequential photographs of the Alg-Na gel electrolyte film degrade in PBS at 60 °C. Photo credit: Hongwei Sheng, Lanzhou University.

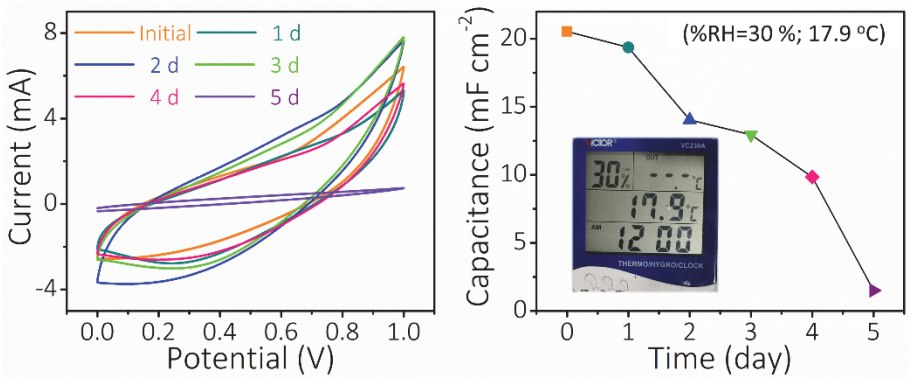

Fig. S14. Electrochemical stability of the encapsulated supercapacitors in open ambient environment (%RH=30 %; 17.9 °C). Photo credit: Hongwei Sheng, Lanzhou University.

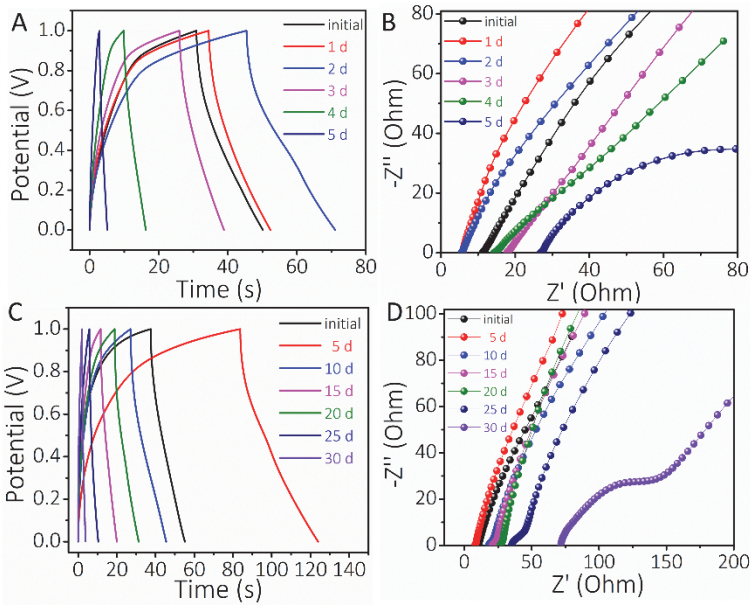

Fig. S15. GCD curves and EIS plots of the encapsulated supercapacitors in PBS. For **(A–B)** a short period of time and (**C–D**) a long period of time in PBS solution at 37 °C, respectively.

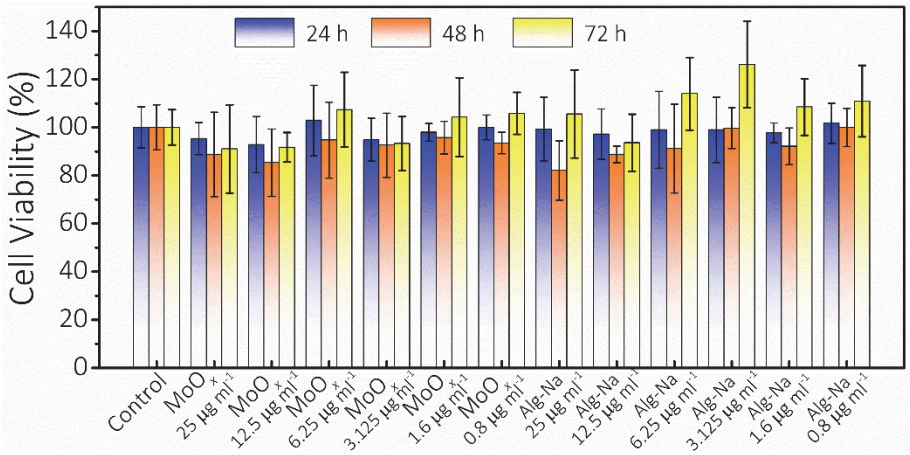

Fig. S16. MTT analysis of the cultured HEC-1-A cells. The error bar represents a standard deviation.

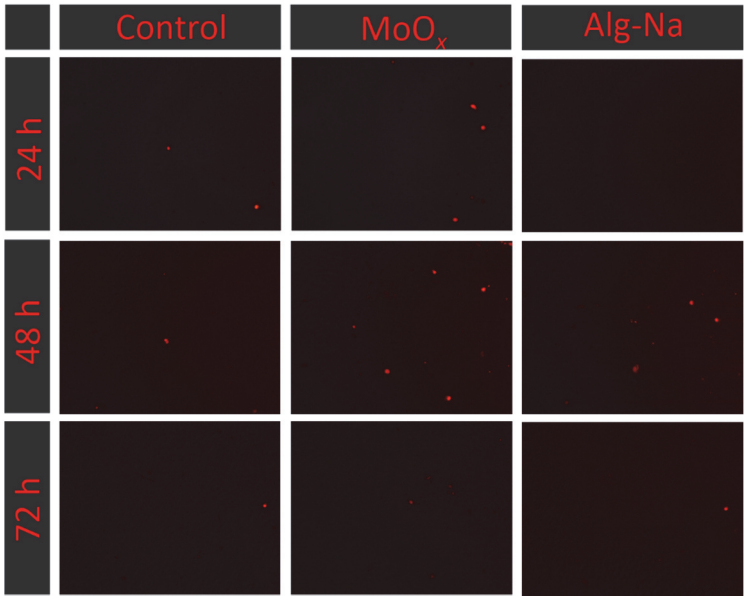

Fig. S17. Fluorescent images of the cell viability. The red dots (PI) represent dead HEC-1-A cells.

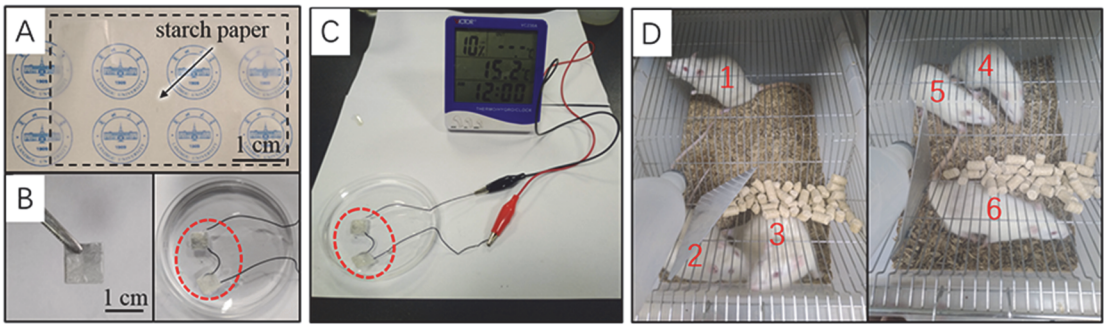

Fig. S18. Digital photographs of the encapsulated supercapacitors and *in vivo* implantation experiments. (A) The transparent starch paper, and **(B)** the encapsulated supercapacitors. **(C)** Demonstration of driving an electronic thermometer using the encapsulated supercapacitors in series in PBS solution. **(D)** *In vivo* implantation experiments were performed in the dorsal subcutaneous region of SD rats (six parallel experiments). Photo credit: Hongwei Sheng, Lanzhou University.

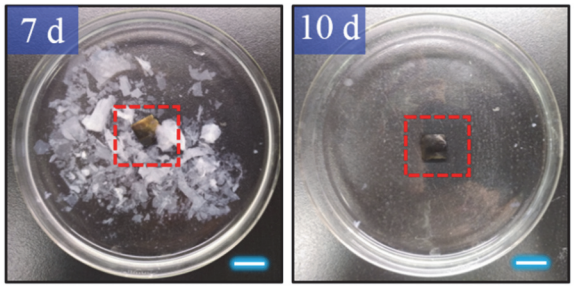

Fig. S19. Digital photographs of the encapsulated supercapacitor in PBS solution at 85 °C. **(A)** After 7 days. **(B)** After 10 days. Scale bar: 1 cm. Photo credit: Hongwei Sheng, Lanzhou University.

	Mo $3d_{3/2}$				Mo $3d_{5/2}$			
	Mo^0 (231.8)	Mo^{4+} (233.2)	Mo^{5+} (234.3)	Mo^{6+} (235.7)	Mo^0 (228.7)	Mo^{4+} (230.1)	Mo^{5+} (231.2)	Mo^{6+} (232.6)
0.4 V	3.05%	9.55%	2.76%	20.8%	15.40%	5.62%	10.81%	32.01%
0.6 V	15.27%	15.04%	2.12%	41.95%	—	—	1.68%	23.94%
0.8 V	10.14%	17.19%	3.6%	40.14%	—	—	3.3%	25.63%
1.0 V	9.5%	23.51%	3.7%	39.54%	—	—	2.6%	21.05%

Table S1. The specific percentages of Mo valence states for MoO_x electrodes anodized at different potential windows.

Electrode Materials	Electrolyte	Thickness	Operation Voltage	Workable Time In Water	Degradable	Capacitance (mF cm^{-2})	Energy Density (μWh cm^{-2})	Power Density (mW cm^{-2})	Ref.
MnO_2@Si nanowires	Li-ion doped ionic liquid	——	2.2 V	——	——	13	9.1	0.388	[37]
Au-MnO_2-Au	PVA/$LiClO_4$	~ 1.6 μm (electrode)	0.8 V	——	——	11.9	1.1	0.1	[36]
Metallic Mo	NaCl@Agarose	~ 160 μm	0.8 V	12 h	Yes	1.6	0.14	1	[14]
Oxidized Mo wire	PVA/PBS	——	0.8 V	——	Yes	4.15	0.37	0.8	[35]
Fe/ZnO	PVA/PBS	~ 50 μm (except substrate)	1.0 V	30 days	Yes	1.1	0.153	0.526	[34]
MoO_x flakes	Sodium alginate	30 μm	1.0 V	30 days	Yes	112.5	15.64	2.53	This work

Table S2. Comparison of the overall performance of supercapacitors with other reported biodegradable supercapacitors.